

Nanoscale

Accepted Manuscript



This is an *Accepted Manuscript*, which has been through the Royal Society of Chemistry peer review process and has been accepted for publication.

Accepted Manuscripts are published online shortly after acceptance, before technical editing, formatting and proof reading. Using this free service, authors can make their results available to the community, in citable form, before we publish the edited article. We will replace this *Accepted Manuscript* with the edited and formatted *Advance Article* as soon as it is available.

You can find more information about *Accepted Manuscripts* in the [Information for Authors](#).

Please note that technical editing may introduce minor changes to the text and/or graphics, which may alter content. The journal's standard [Terms & Conditions](#) and the [Ethical guidelines](#) still apply. In no event shall the Royal Society of Chemistry be held responsible for any errors or omissions in this *Accepted Manuscript* or any consequences arising from the use of any information it contains.

Modelling energy deposition in nanoscintillators to predict the efficiency of the X-ray-induced photodynamic effect

Anne-Laure Bulin,^a Andrey Vasil'ev,^b Andrei Belsky,^a David Amans,^a Gilles Ledoux,^a and Christophe Dujardin^{*a}

Received Xth XXXXXXXXXXXX 20XX, Accepted Xth XXXXXXXXXXXX 20XX

First published on the web Xth XXXXXXXXXXXX 200X

DOI: 10.1039/b000000x

Scintillating nanoparticles (NPs) in combination with X- or γ -radiation have a great potential for deep-tissue cancer therapy because they can be used to generate singlet oxygen in tumours by means of the photodynamic effect. To understand the complex spatial distribution of energy deposition in a macroscopic volume of water loaded with nanoscintillators, we have developed a GEANT4-based Monte Carlo program. We thus obtain estimates of the maximum expected efficiency of singlet oxygen production for various materials, X-ray energies, NP concentrations and NP sizes. A new parameter, η_{nano} , is introduced to quantify the fraction of energy that is deposited in the NPs themselves, which is crucial for the efficiency of singlet oxygen production but has not been taken into account adequately so far. We furthermore point out the substantial contribution of primary interactions taking place in water, particularly under irradiation with high energy photons. The interplay of all these contributions to the photodynamic effect has to be taken into account in order to optimize nanoscintillators for therapeutic applications.

1 Introduction

Scintillators are known to emit visible or UV photons under ionizing radiation. These materials are used as convertors for X-, γ -ray and more generally for ionizing radiations detection.¹ When prepared at nanosizes and properly functionalized they open areas for therapies where light emission triggered by X- or γ -ray excitation within deep tissues is desired. Combining the nanoparticle scintillating property and photosensitizers (PS) grafted on their surfaces, radiotherapy and photodynamic therapy (PDT) can be used together to improve the elimination of deep tumours^{2,3}.

PDT is a non invasive technique based on the photoactivation of an organic molecule called a photosensitizer (PS). Once excited, the PS produces reactive oxygen species including singlet oxygen ($^1\text{O}_2$)⁴⁻⁶. Since the PS becomes cytotoxic only when excited by light emitted at a suitable wavelength, PDT is a highly selective treatment. Nevertheless, the commonly used activation wavelengths in the visible range have a low penetration depth in human tissues (about 6 mm) and the use of PDT is therefore restricted to superficial tumours⁵. The combination of radiotherapy, which requires penetrating X-rays, and PDT consists in using nanoscintillators to locally convert X-

rays into light, which then excites the PS and thus generates $^1\text{O}_2$. This concept was introduced by Chen *et al* in 2006² and recent studies have demonstrated an experimental proof of concept of this effect⁷⁻¹¹. A first numerical estimation of its efficiency was put forth by Morgan *et al*¹². However, the proposed approach is restrictive and over-estimates the energy deposition in nanoparticles since energy relaxation in scintillators involves complex processes^{13,14} including primary and secondary excitations having migration distances larger than the nanoparticle size¹⁵⁻¹⁸. Such migration distances suggest that energy is shared between the nanoparticle and its surroundings. The energy deposited in the particle may lead to scintillation and then to activation of the PS, while the energy deposited outside of the particle may locally increase the deposited dose in surrounding tissues.¹⁹ The latter effect is known as radiosensitization and involves loading high density NPs into tumours to increase the dose absorption leading to DNA and other damages of the cancer cells²⁰. This effect is mainly studied with injection of gold particles because of the high atomic number of this material that highly increases cross section of the photoelectric effect.²¹⁻²⁵

In this contribution, we use Monte Carlo simulations to numerically estimate the spatial energy distribution resulting from the interaction between the X-ray photon and the NP which drives the PDT and radiosensitization efficiencies. These simulations can then be used to optimize the nano-hybrid systems for cancer therapy, which is why we have studied selected materials which have already been considered for proof of concept demonstrations or that we consider

^a Institut Lumière Matière, UMR5306, Université Claude Bernard Lyon1-CNRS, bâtiment Kastler, 10 rue Ada Byron 69622 Villeurbanne Cedex, France. Fax: (33) 472 431 130; Tel: (33) 472 448 336; E-mail: christophe.dujardin@univ-lyon1.fr

^b Skobeltsyn Institute of Nuclear Physic, Lomonosov Moscow State University, Leninskie 1 (2), Moscow, 119991, Russia.

to be of potential interest. We first selected three well known scintillator compositions (when doped either with Eu^{3+} or Tb^{3+}): gadolinium oxide (Gd_2O_3), gadolinium oxysulfide ($\text{Gd}_2\text{O}_2\text{S}$) and lutetium oxide (Lu_2O_3). These materials are dense and their scintillation yields in bulk are among the highest known.²⁶ In addition, when properly capped, the simple oxides have already demonstrated to have an appropriate pattern of biodistribution after injection²⁷. $\text{Gd}_2\text{O}_2\text{S}$ nanoparticles have already been successfully synthesized and stabilized in water²⁸. $\text{LaF}_3:\text{Tb}^{3+}$ has also been used for demonstration as well as $\text{LaF}_3:\text{Ce}^{3+}$.^{7,9} We also performed the calculations on two efficient light emitters: cadmium selenide (CdSe)^{29,30} and Indium Phosphate (InP)^{31,32}. CdSe has already demonstrated some scintillation properties³³ and has been proposed to obtain a PDT effect.^{34,35} A recent publication of Lemon *et al.*³⁶ reports an efficient transfer in a system made of CdSe quantum dots conjugated with porphyrins. In the following sections, the calculations are detailed for Gd_2O_3 , and results for all other materials are summarized in the last part.

2 Methods

To estimate the spacial distribution energy deposition in a nanostructured volume, we used Monte Carlo simulations based on the GEANT4 toolkit (version 4.9.6 patch 02) with the Livermore low energy package which is the most suitable package for low energy deposition in inorganic materials. The system to be analyzed is a sphere of water representing the tumour and having a volume V_{tum} , which is loaded with nanoscintillators at a concentration of C . The absorption of the considered volume being weak, the program is divided in two parts in order to improve the number of events leading to interactions. The first one calculates the energy distribution of secondary electrons and photons generated by interaction of γ -rays with matter. The second step calculates the energy deposited in nanoparticles by the electrons and X-rays randomly generated in the source NP.

For the first program, the geometry consists of a rod-like structure of scintillating material with an area of 1 nm^2 and 1 mm length. This rod is placed at the center of the *world* represented as an empty box, with size dimensions of 15 cm - chosen much bigger than ones of the rod. A sensitive detector was placed around the rod allowing to histogram all the secondary particles created by the interaction of γ -rays with the matter. Incident radiation consists of a monoenergetic beam irradiating the center of the 1 nm^2 surface of the rod.

To achieve a volume ratio in the range of $C \approx 10^{-3}$ by distributing 10 nm diameter NPs within a macroscopic volume $V_{\text{tum}} \approx \text{few } \text{mm}^3$, we need to place about 10^{15} NPs, which is far above the computational memory capacity. For the second program, the geometry is therefore composed of a source NP, surrounded by a sphere having a diameter of $1 \mu\text{m}$ loaded

with randomly distributed NPs. This sphere is surrounded by several shells regularly spaced with distance h and a thickness equal to the NP diameter. We optimized the geometry to limit the fluctuations in the deposited energy and reached the final geometry: the shells are regularly spaced by a distance h , the first one has an inner radius of $1 \mu\text{m} + h/2$ and the center of the whole set of shells is shifted from the distance $h/2$ in one given direction. More details and justifications about this choice are given in the supplementary informations (SI1). The distance h and the number of shells were calculated by keeping the same C ratio. The selection of the C values is discussed later in this contribution.

3 Results and Discussion

3.1 Local dose excess for high-Z materials

The primary interaction of γ -rays of energy E with matter leads to ionization of atoms by the photoelectric effect or by inelastic Compton scattering. The probability of each process depends on the atomic number (Z) of the considered element. For instance, the photoelectric cross section varies approximately as $(Z/E)^3$ except for energies about the absorption edges. Pair production may also occur for energies above 1.022 MeV but our calculations will use energies below this limit.

In order to estimate the local excess of transferred energy in high-Z material regarding tissues, the mass energy absorption coefficient $\frac{\mu_{\text{en}}}{\rho}$ is used. μ_{en} is the absorption coefficient while ρ is the mass density of the material. Figure 1a) represents the evolution of this coefficient - $\frac{\mu_{\text{en}}}{\rho}$ - as a function of the γ -ray energy for Gd_2O_3 , Lu_2O_3 , LaF_3 , CdSe as well as for water. By dividing the values of $\frac{\mu_{\text{en}}}{\rho}$ for each high-Z material by the $\frac{\mu_{\text{en}}}{\rho}$ values of water (Fig. 1b), we directly obtain the ratio of the enhancement of the local transferred energy for the selected materials. According to this data, the maximum energy transfer enhancement occurs for energies around $40 - 60 \text{ keV}$. This demonstrates the well known interest of loading high-Z material into tumours and the paper published by Morgan *et al.*¹² nicely describes this effect for several scintillators. However, an ensemble of nanoparticles in liquid is similar to a composite medium and this mass energy absorption coefficient cannot be applied directly to the energy deposited in the nanoparticles. Indeed, secondary particles, such as δ electrons, Auger electrons and X-ray fluorescence photons exhibit migration distances that are, in most cases, larger than the nanoparticle size¹⁶. As a consequence, a fraction of the transferred energy given by the previous attenuation calculation will actually escape from the nanoparticle and the deposited energy is thus shared between the water and the nanoparticles. We therefore aim to determine the spatial distribution of deposited energy

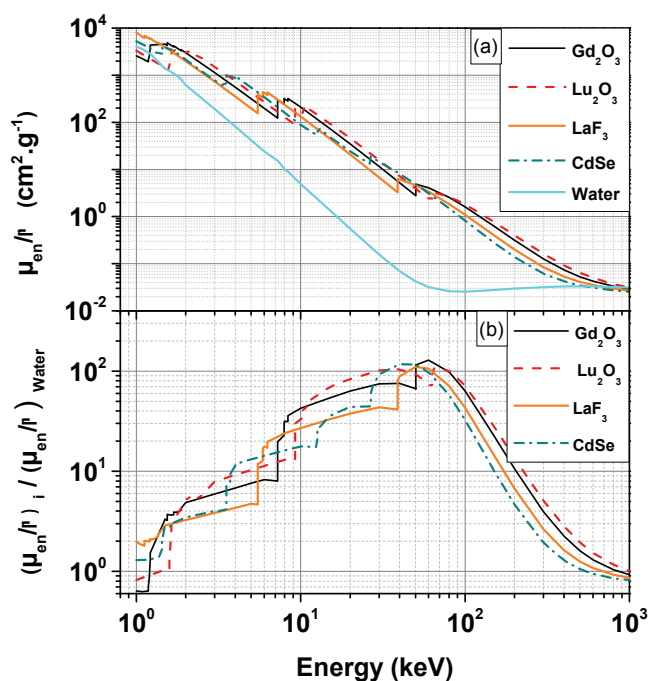


Fig. 1 a) Mass energy coefficient $\frac{\mu_{en}}{\rho}$ as a function of the X-ray or γ -ray energy for three scintillating materials (Gd₂O₃, Lu₂O₃, LaF₃), for CdSe as well as for water. b) Ratio of the considered material compared to water for the same material thickness. These values have been obtained using the NIST database.³⁷

in the volume surrounding the nanoparticle where the primary interaction occurs in order to extract limitations of the energy deposition efficiencies. We performed Monte Carlo GEANT4 calculations, using the Livermore physics list optimized for low energies and a multistep analysis described in the following sections.

3.2 Absorption of high energy γ : spectra of primary particles

The spatial distribution of deposited energy depends on the energy of the particles generated by the γ interaction with matter. Histogramming the energies of primary particles - electrons and photons - generated by the interaction of the γ photon in the matter is therefore the first step. Such a spectrum depends on the energy of the interacting γ -ray and on the material composition. The absorption efficiency is higher for dense material than for water but with commonly used concentrations, NPs occupy a small fraction of the total volume^{22,38}. This means that the interaction between the γ photon and the matter can occur either in the NPs or in water. We have then considered primary particles generated after an interaction in Gd₂O₃ and in water. The fraction of interactions

that occur in Gd₂O₃ and in water is discussed later.

Figure 2a represents the number of generated electrons at a given energy E due to the interaction between a 500 keV γ photon and Gd₂O₃. The histogram was normalized to the number of interacting γ photons (10⁶ events) to obtain the distribution function. Such a typical spectrum can be described as follows: The high energy lines are due to a photoelectric interaction with an atom that remains excited and whose relaxation can induce Auger electrons (low energy lines) as well as X-ray fluorescence photons (escaped X-rays). These lines depend on the energetic characteristics of the material constituents (K, L, M... thresholds). The continuum arises from the Compton effect, where only a part of the initial energy is transferred to an electron from an outer atomic shell. We write the general form of such an electron spectrum which depends on the energy of incident γ -ray and of the material in which the interaction occurs (here Gd₂O₃) as $S_{Gd}^e(E_\gamma, E)$.

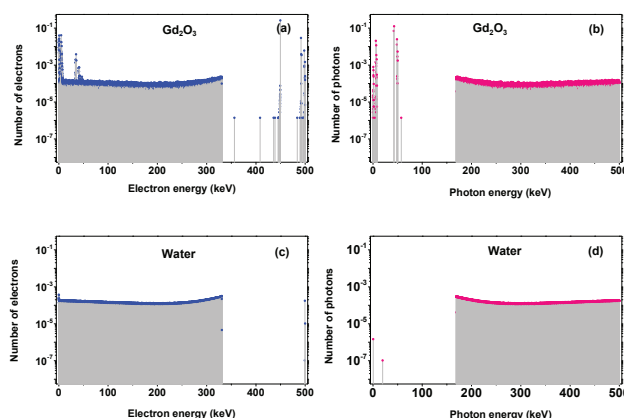


Fig. 2 Histograms correspond to the normalized number (per interaction γ -photon) of primary particles generated after interaction with a 500 keV γ photon in Gd₂O₃, (a) electrons and (b) photons, and in water, (c) electrons and (d) photons. Note that the sum over all events is larger than 1 because some interactions produce multiple electrons. Nevertheless we checked that the normalization condition is respected: $E_\gamma = \sum_i S^e(E_\gamma, E_i) \cdot E_i + \sum_j S^p(E_\gamma, E_j) \cdot E_j$

Figure 2b represents the distribution function of primary photons, $S_{Gd}^p(E_\gamma, E)$, generated after the interaction with a 500 keV γ photon with Gd₂O₃. The low energy photon lines correspond to the X-ray fluorescence involved in atomic relaxation of deep holes. The energy continuum corresponds to Compton scattered γ -rays.

The histograms presented in Figs. 2c and 2d are the same distribution functions, $S_{wat}^e(E_\gamma, E)$ and $S_{wat}^p(E_\gamma, E)$, but considering an interaction in water instead of Gd₂O₃. Because

water is composed of light elements, Compton scattering is the main interaction and the photoelectric effect becomes negligible. As a consequence neither discrete high energetic electrons nor low energy Auger electrons and X-ray fluorescence resulting from atomic relaxation appear.

3.3 Energy deposited in the "source" nanoparticle

Once we obtain the histograms of electron and photon distribution functions, we aim to evaluate the fraction of energy deposited within the NP where the γ photon interacted - called the "source NP". For this second step, we developed another program to follow step by step each primary particle and to plot the spatial distribution of the deposited energy in and outside the NP. In this program, a Gd_2O_3 NP is simulated as a sphere, placed at the center of a bigger water sphere. The primary particles (electrons or photons) are randomly (in initial position and direction) generated within the Gd_2O_3 NP. The fraction (in %) of energy deposited in the source nanoparticle by primary and secondary electrons (resp. photons) as a function of their initial energy is $\eta^e(E)$ (resp. $\eta^p(E)$). Examples of such curves are given in Fig. 3 for three different NP diameters: 10, 40 and 100 nm. Even for the biggest NP, the deposited energy decreases very quickly when the electron energy increases. Two illustrations of spatial distribution of energy deposition are presented in the case of an electron initial energy of 2 keV (Fig. 3.1) and 10 keV (Fig. 3.2) generated in a 100 nm diameter Gd_2O_3 NP. On these visualizations, the NP is represented by a blue sphere, the electron trajectories by red lines and the hits by yellow dots. For each case, the energy depositions per unit radial distance are plotted as a function of the normalized distance to the NP center. Even for these low energy electrons, a large amount of energy leaves the NP and is deposited in the surrounding medium. To calculate the energy deposited in the NP by the primary electrons and photons generated after interaction of a γ photon in the source NP, we sum over all bins i (electrons) and j (photons) corresponding the energies $E_{i/j}$ (Fig. 2):

$$E_{\text{source}} = \sum_i S_{\text{Gd}}^e(E_\gamma, E_i) \cdot \eta^e(E_i) \cdot E_i + \sum_j S_{\text{Gd}}^p(E_\gamma, E_j) \cdot \eta^p(E_j) \cdot E_j \quad (1)$$

The results obtained for a Gd_2O_3 NP of 100 nm diameter are presented in Table 1, which summarizes the amounts of energy deposited by electrons and photons within the source NP after interaction of a γ photon with an energy E_γ (from 100 to 500 keV).

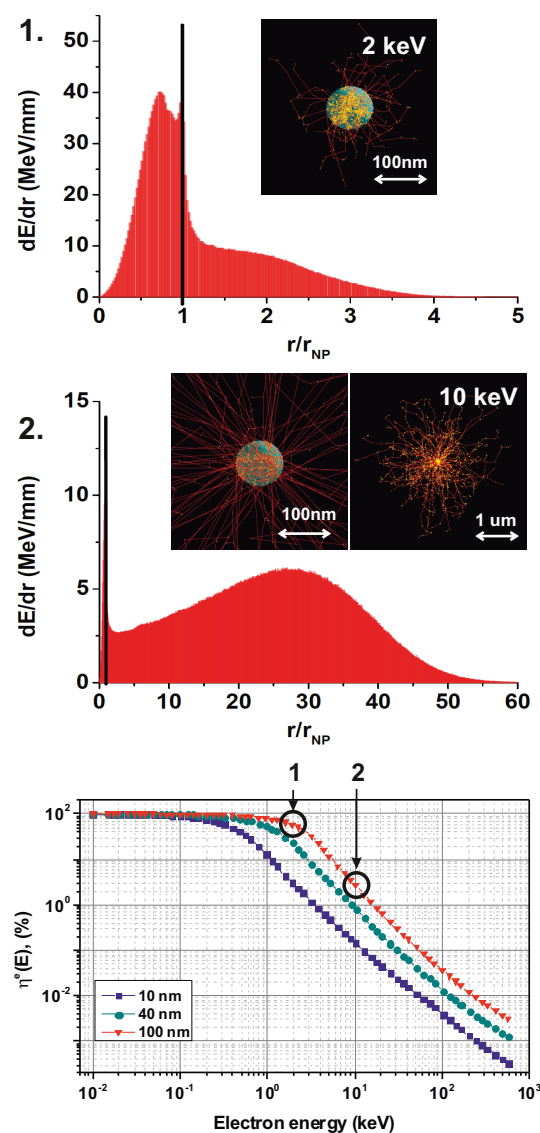


Fig. 3 Top: deposited energy per unit of normalized radial distance from the center of the NP (diameter of 100 nm of Gd_2O_3) for 1- 2 keV electrons and 2- 10 keV electrons. Visualisation of the spatial distribution of the deposited energy are shown as insets. Bottom: Percentage of deposited energy per electron generated in a Gd_2O_3 nanoparticle for three different diameters, as a function of the primary electron energy.

3.4 Influence of the concentration

The previous calculation points out that the fraction of deposited energy in a source NP Gd_2O_3 interacting with a γ photon is rather small. In addition, the spatial distribution of the deposited energy (see Fig. 3) clearly shows that energy

Table 1 Energy deposited (in keV) in a NP with a diameter of 100 nm by electrons (E_{source}^e) and photons (E_{source}^p) for five initial energies of the interacting γ -ray.

E_γ (keV)	100	200	300	400	500
E_{source}^e (keV)	1.07	0.88	0.67	0.49	0.37
E_{source}^p (eV)	2.4	2.0	1.5	1.1	1.1

deposition distances might reach several micrometers, which suggests that depending on the NP concentration, secondary particles may be involved in the energy deposition process. As a consequence we have to take surroundings NPs into account in our simulations.

3.4.1 Multi-NP tumour model. The system we are now studying is a macroscopic volume called V_{tum} , that represents a tumour. V_{tum} is supposed to be a sphere filled with water and loaded with Gd_2O_3 NPs. We consider a radius of 2.8 mm because this corresponds to the smallest volume able to contain all the secondary particles induced by primary electrons resulting from an interaction with γ -rays of energies up to 500 keV. Furthermore, such a size is within a reasonable order of magnitude in agreement with volumes used to describe tumour models in the literature.³⁹ We consider a first interaction occurring at the center of this volume. The NPs concentrations were chosen using data from Hainfeld²¹ and McMahon³⁸ who performed experimental measurements of radiosensitization enhancement effect in presence of gold NPs. From the values given in these contributions, we estimated some realistic particle volumic concentrations quantified by the ratio $C = V_{\text{occupied}}/V_{\text{tum}}$. We considered thus two different C values equal to $7 \cdot 10^{-3}$ and $2 \cdot 10^{-3}$ that corresponds to around 52 mg.mL^{-1} and 15 mg.mL^{-1} of Gd_2O_3 , respectively. The concentrations of in vitro experiments may be lower but in this range of concentrations we expect a linear evolution of the deposited energy with the concentration. We performed the calculations for two different diameters, 10 and 100 nm, that correspond to diameters of NPs delivered via intravenous injection and via intratumoural injection respectively.⁴⁰ As described in the method section, we therefore divide the tumour volume into two zones with respect to the NP that absorbs the γ -photon: on one hand, there is the near zone, for which we fully take into account the interaction with a random distribution of secondary NPs. NPs far away from the primary absorber, on the other hand, are introduced in the model as spherically symmetric shells of Gd_2O_3 with appropriate thicknesses and spacing.

Using this model, the fraction of deposited energy, now written as a function of the initial primary electron energy E , can be deduced $\eta_c^e(E)$ ($\eta_c^p(E)$ for primary photons). The subscript c indicates that this attenuation depends on the concentration C . Fig. 4 illustrates how the energy is shared among

the various considered part of the geometry. Note first that the minimum observed around 8 keV is due to edge effect of the selected geometry and has no physical sense (See SI1). We can clearly see that the fraction of deposited energy in the source NP is negligible for electron energy over a few keV. Note also that the deposited energy is a mean value over a huge number of events and that from event to event we have natural fluctuation of energy deposition. In the inset, we illustrate the calculated distribution of energy deposition event for a primary electron having an energy of 250 keV. Here, the mean deposited energy is 5 keV and the full width half maximum corresponding to the spread in energy deposition is about 3 keV.

3.4.2 Discussion of the first interaction. As mentioned, the primary interaction with the γ -ray can occur in water or in a Gd_2O_3 NP. According to the Beer-Lambert equation, the fraction (α) of γ -rays that interact with a system containing Gd_2O_3 NPs can be obtained considering the attenuation coefficient μ_{att} and the equivalent thicknesses for either Gd_2O_3 or water (from the NIST table³⁷). Despite the attenuation coefficient of Gd_2O_3 being larger than the attenuation coefficient of water, most of the interactions occur in water because of the small volume fraction occupied by the nanoparticles. β_{wat} and β_{Gd} that are presented in Table 2, quantify the positioning of γ photon interaction probabilities among the two materials. They point out the crucial role of absorption in water that also needs to be considered for the calculation of energy deposition in the scintillator.

Table 2 α is the fraction of γ photons interacting in the tumour (expressed in %). The columns Gd_2O_3 and water indicate how the interaction probabilities are distributed between the two materials (β_{wat} and β_{Gd}).

E_γ (keV)	$C = 2 \cdot 10^{-3}$			$C = 7 \cdot 10^{-3}$		
	β_{Gd}	β_{wat}	$\alpha(\%)$	β_{Gd}	β_{wat}	$\alpha(\%)$
100 keV	0.20	0.80	7.6	0.45	0.55	11.2
200 keV	0.05	0.95	5.4	0.16	0.84	6.0
300 keV	0.03	0.97	4.5	0.09	0.91	4.8
400 keV	0.02	0.98	4.1	0.06	0.94	4.2
500 keV	0.02	0.98	3.7	0.05	0.95	3.8

3.4.3 Calculation of the energy deposited in each material. To estimate the total energy deposition, we need to consider all generated primary electrons and photons, whether the first interaction occurs in water or in Gd_2O_3 . Because the energy spectrum of the primary particles generated is different when the interaction occurs in Gd_2O_3 and in water, the calculation of deposited energy in the scintillator per interacting

Table 3 Total energy deposited (in keV) in Gd₂O₃ and in water after the interaction of one γ photon in the tumour. NPs of 10 and 100 nm diameter are considered with occupation ratios equal to $2 \cdot 10^{-3}$ and $7 \cdot 10^{-3}$, respectively. For comparison, the deposited energy in water in the case of particle free tumour ($C=0$) are respectively (in keV) 15.87, 44.74, 82.74, 126.22 and 173.44 for interacting photons having the specified energy values given in the table from 100 keV to 500 keV

$C = 2 \cdot 10^{-3}$	10 nm		100 nm	
	Gd ₂ O ₃	Water	Gd ₂ O ₃	Water
E_γ (keV)				
100 keV	0.23	25.50	0.91	24.93
200 keV	0.30	49.67	0.79	49.20
300 keV	0.51	85.37	0.92	84.97
400 keV	0.79	127.45	1.13	127.10
500 keV	1.10	173.85	1.41	173.52
$C = 7 \cdot 10^{-3}$	10 nm		100 nm	
	Gd ₂ O ₃	Water	Gd ₂ O ₃	Water
E_γ (keV)				
100 keV	0.95	38.49	2.12	37.36
200 keV	1.21	59.62	1.94	59.07
300 keV	1.84	90.99	2.47	90.55
400 keV	2.70	130.26	3.29	129.81
500 keV	3.71	174.93	4.28	174.29

γ -ray takes the following form:

$$E_{\text{total}} = \sum_{k=\text{wat,Gd}} \beta_k \cdot \left(\sum_i S_k^e(E_\gamma, E_i) \cdot \eta_c^e(E_i) \cdot E_i + \sum_j S_k^p(E_\gamma, E_j) \cdot \eta_c^p(E_j) \cdot E_j \right) \quad (2)$$

Similarly, we can also estimate the energy deposition in the water. Table 3 presents the final results obtained for 10 and 100 nm diameter NPs of Gd₂O₃ placed in water with two different occupation ratios ($2 \cdot 10^{-3}$ and $7 \cdot 10^{-3}$). As indicated above, the obtained results represent a statistical average of the deposited energy amount. The respective contributions of primary interactions in water and in the NP can be evaluated. As an illustration for $C = 7 \cdot 10^{-3}$ and 10 nm diameter NP, 3.41 keV of the 3.71 keV which are statistically deposited in the NP is due to primary interactions occurring in water (92%), pointing out the crucial role of this effect.

We restricted the calculation to 500 keV because of computing time. For energies larger than 200-300 keV, a linear behaviour can be seen from table 3. These energies are far above the highest energy absorption edge (The K-edge of Gd is around 50.2 keV). Therefore, we consider the behaviour as linear at higher energies. Nevertheless, some sublinearities are expected over 500 keV if the tumour size is kept at 2.8 mm, since such a size has been selected to contain the secondary electrons. For energies slightly larger than 2.511 keV, a few events leading to pair creation might occur, but the probability remains weak. We consider that the energy deposition effi-

ciency order of magnitude can then be extrapolated from the results calculated at 500 keV.

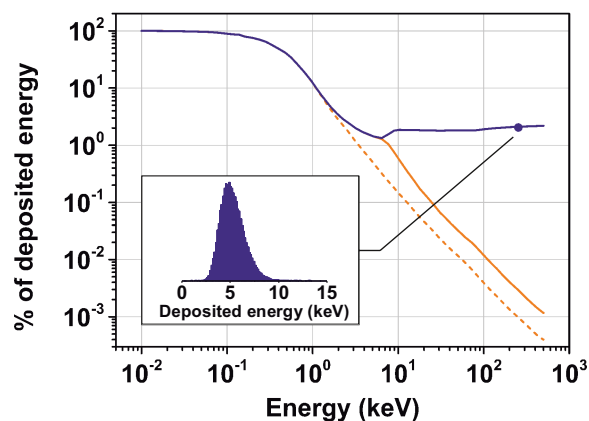


Fig. 4 Energy deposition in the various parts of the multi-NP tumour model as a function of the primary electron energy. The calculations are performed for 10 nm diameter NPs of Gd₂O₃ placed in water with the occupation ratio $C = 7 \cdot 10^{-3}$. Dashed orange: source NP; Solid orange: Source NP + first sphere of diameter of $1 \mu\text{m}$ containing NPs; Solid purple: the whole system. The inset presents an histogram of energy fluctuations around the mean value for a primary electron of energy 250 keV.

3.4.4 PDT activation. X-ray induced PDT requires that the scintillator, here Gd₂O₃, be in its excited state, which can then either emit light or excite the photosensitizer through radiative or non radiative transfer (FRET)⁸. Once activated, the photosensitizer generates a reactive oxygen species such as singlet oxygen, the main cytotoxic agent involved in the PDT process. Based on the previous discussion, we adapted the formula proposed by Morgan et al. to estimate the efficiency of the PDT activated by x-rays.¹² $N_{1\text{O}_2}$, the number of generated $^1\text{O}_2$ per interacting X photon can be obtained as follows:

$$N_{1\text{O}_2} = \eta_{\text{nano}} \cdot \Phi_{\text{scinti}} \cdot E_\gamma \cdot \Phi_{\text{transfer}} \cdot \Phi_\Delta,$$

where Φ_{scinti} corresponds to the scintillation yield of the considered scintillator when ungrafted (expressed in number of photons per keV), E_γ is the energy of the interacting photon (keV), Φ_{transfer} is the transfer efficiency from the nanoscintillator to the photosensitizer and Φ_Δ is the singlet oxygen production efficiency once the photosensitizer is activated. We demonstrated above that the spacial distribution of energy relaxation in the mixed media means that only a fraction of the initial energy is deposited in the scintillating nanoparticles and we therefore introduce η_{nano} as this fraction. Note that our calculations show a significant deposited energy in the scintillator

despite the primary interaction occurring in water. η_{nano} takes into account this contribution to the total energy deposited in the scintillating material and is calculated for a given occupation ratio of the tumour. As an illustration, in the case of 10 nm nanoparticles distributed in the tumour with an occupation ratio of $7 \cdot 10^{-3}$, a 100 keV γ -ray that interacts in the tumour finally deposits in average 950 eV leading to an estimated $\eta_{\text{nano}} = 0.95\%$. When the occupation ratio decreases to $2 \cdot 10^{-3}$, the value of η_{nano} goes down to 0.23% pointing out that this parameter is almost proportional to the NP concentration (in this low concentration range). The values of η_{nano} are presented in the supplementary Information (SI3) for Gd_2O_3 NPs of 10 and 100 nm diameter, distributed in the tumour with the occupation ratios of $2 \cdot 10^{-3}$ and $7 \cdot 10^{-3}$.

Φ_{Δ} has already been measured and the highest values are about 0.8¹². To estimate the physical limits due to energy deposition, we consider the most favorable case where Φ_{transfer} is equal to 1. The value of Φ_{scinti} is strongly material dependent. The best values obtained in modern scintillators for ionizing radiation detection are in the order of 10^5 photons per MeV (about 97000 photons/MeV for BaBrI:Eu^{2+}).⁴¹ Nevertheless, such a high value is given for bulk single crystal and biocompatibility of this compound is unknown. For more common materials already existing as NPs such as Gd_2O_3 we consider as more reasonable a scintillation yield for bulk materials of about 15000 photons per MeV²⁶.

From these assumptions we deduce that around 12000 $^1\text{O}_2$ molecules may be produced per MeV of energy deposited in the nanoscintillator. As an illustration, in the case of a tumour containing 10 nm NPs distributed with an occupation ratio of $7 \cdot 10^{-3}$ irradiated by 500 keV γ photons, the average value of energy deposited in the Gd_2O_3 NPs is 3.71 keV (Table 3). It gives an average number of $^1\text{O}_2$ molecules activated per interacting photon equal to 44. This number of $^1\text{O}_2$ molecules activated per interacting photon might appear to be small, that is why this therapy has to be considered as combined with radiotherapy, for which the fluences are intense. In addition, energy deposition in the tumour (the water in our model) induces the well known radiosensitization effect^{19,24,25}, that corresponds to a local excess of the dose deposited inside the tumour volume compared to in healthy tissues due to the presence of NPs. The potential of this treatment is then based on the combined effect of radiotherapy, radiosensitization and PDT.

3.5 Calculation for other compounds

Because efficiency of the PDT induced by X-ray radiation depends on many factors such as biodistribution after injection, toxicity, scintillation yield, efficiency of transfer toward photosensitizers, several material types might compete each others. We stress here the energy deposition of several potential nanoscintillators for 100 and 500 keV irradiation, for a par-

Table 4 Energy deposited in matter (keV) for one γ photon interaction in a tumour of volume V_{tum} loaded with 10 nm diameter NPs, with an occupation ratio of $7 \cdot 10^{-3}$. The absorption of the photons is also calculated for the two considered energies.

$E_{\gamma} = 100 \text{ keV}$	Abs.(%)	E_{matter}	η_{nano} (%)
Gold	29.0	2.59	2.59
Lu_2O_3	14.5	1.22	1.22
Gd_2O_3	11.2	0.95	0.95
Lu_2SiO_5	12.0	0.92	0.92
$\text{Gd}_2\text{O}_2\text{S}$	11.0	0.94	0.94
$\text{Lu}_3\text{Al}_5\text{O}_{12}$	10.5	0.81	0.81
LaF_3	8.69	0.66	0.66
CdSe	7.85	0.55	0.55
InP	7.74	0.46	0.46
Water	6.15		
$E_{\gamma} = 500 \text{ keV}$	Abs.(%)	E_{matter}	η_{nano} (%)
Gold	4.41	7.92	1.58
Lu_2O_3	3.95	4.46	0.89
Gd_2O_3	3.84	3.71	0.74
Lu_2SiO_5	3.87	3.87	0.77
$\text{Gd}_2\text{O}_2\text{S}$	3.85	3.74	0.75
$\text{Lu}_3\text{Al}_5\text{O}_{12}$	3.84	3.87	0.77
LaF_3	3.79	3.40	0.68
CdSe	3.77	3.05	0.61
InP	3.76	2.72	0.54
Water	3.66		

ticular configuration: 10 nm diameter NPs distributed in the tumour with an occupation ratio of $7 \cdot 10^{-3}$ (Table 4). Despite corresponding to particular conditions, the obtained results can be extrapolated to other cases in order to extract order of magnitudes. Indeed, we saw previously, that the deposited energy is not that much dependent to particle size when keeping the same occupation ratio. We also expect a linear dependence on concentration in this range. For larger tumour volumes, taking into account the small absorption coefficient, the absorption varies almost linearly with the considered volume. Regarding energy deposition, the V_{tum} selected was chosen to contain all the secondary electrons, increasing the volume will only affect the deposited energy due to secondary X-rays, which linearly depends on the volume. The respective fraction of energy deposition due to secondary electrons and X-rays are presented in the supplementary Information (SI2). The dependence with energy of incident γ -rays is less direct and would require specific calculations. We nevertheless see that from 100 keV to 500 keV, the deposited energy in the nanoparticles is multiplied by about 3.6 in the case of Lu_2O_3 and by 5.9 for InP .

4 Conclusion

In conclusion, we have shown that the spatial energy distribution between the nanoscintillators and the surrounding media occurring during the energy relaxation cascade of an interacting X- or γ -ray leads to a significant loss regarding the light emission efficiency and thus the photodynamic effect. On the other hand, we point out that a significant fraction of energy is deposited within the NPs despite the primary interaction occurring in the surrounding media. Taking into account of these effects, a new loss parameter η_{nano} has been introduced and numerically estimated using Monte Carlo simulations for various nanoscintillator types in terms of composition, size and concentration. This knowledge can be used to quantify the expected number of $^1\text{O}_2$ generated in the frame of therapy combining radiotherapy and photodynamic effect.

5 Acknowledgement

The "Agence Nationale de la Recherche" (ANR) is thanked for its support of the PDTX program (ANR-10-NANO-0009).

References

- M. Weber, *J. Lumin.*, 2002, **100**, 35–45.
- W. Chen and J. Zhang, *J. Nanosci. Nanotechnol.*, 2006, **6**, 1159–1166.
- P. Juzenas, W. Chen, Y.-P. Sun, M. A. Neto Coelho, R. Generalova, N. Generalova and I. L. Christensen, *Adv. Drug Deliver. Rev.*, 2008, **60**, 1600–1614.
- T. Dougherty, C. Gomer, B. Henderson, G. Jori, D. Kessel, M. Korbelik, J. Moan and Q. Peng, *J. Natl. Cancer Inst.*, 1998, **90**, 889–905.
- P. Hasan, B. Ortel, A. Moor and B. Pogue, *Holland-Frei Cancer Medicine*, BC Decker, 6th edn, 2003, ch. 40, pp. 605–622.
- P. Agostinis, K. Berg, K. A. Cengel, T. H. Foster, A. W. Girotti, S. O. Gollnick, S. M. Hahn, M. R. Hamblin, A. Juzeniene, D. Kessel, M. Korbelik, J. Moan, P. Mroz, D. Nowis, J. Piette, B. C. Wilson and J. Golab, *Ca Cancer J. Clin.*, 2011, **61**, 250–281.
- Y. Liu, W. Chen, S. Wang and A. G. Joly, *Appl. Phys. Lett.*, 2008, **92**, 043901.
- A.-L. Bulin, C. Truillet, R. Chouikrat, F. Lux, C. Frochot, D. Amans, G. Ledoux, O. Tillement, P. Perriat, M. Barberi-Heyob and C. Dujardin, *J. Phys. Chem. C*, 2013, **117**, 21583–21589.
- X. Zou, M. Yao, L. Ma, M. Hossu, X. Han, P. Juzenas and W. Chen, *Nanomedicine*, 2014, 1–13.
- D. R. Cooper, K. Kudinov, P. Tyagi, C. K. Hill, S. E. Bradforth and J. L. Nadeau, *Phys. Chem. Chem. Phys.*, 2014, **16**, 12441–12453.
- L. Ma, X. Zou and W. Chen, *J. Biomed. Nanotechnol.*, 2014, **10**, 1501–1508.
- N. Y. Morgan, G. Kramer-Marek, P. D. Smith, K. Camphausen and J. Capala, *Radiat. Res.*, 2009, **171**, 236–244.
- P. Rodnyi, P. Dorenbos and C. VanEijk, *Phys. Status Solidi B*, 1995, **187**, 15–29.
- M. Weber, *Nucl. Instrum. Meth. B*, 2004, **527**, 9–14.
- A. Vasilev, *Nucl. Instrum. Meth. B*, 1996, **107**, 165–171.
- A. Belsky, R. Glukhov, I. Kamenskikh, P. Martin, V. Mikhailin, I. Munro, C. Pedrini, D. Shaw, I. Shpinkov and A. Vasilev, *J. Electron Spectrosc.*, 1996, **79**, 147–150.
- R. Kirkin, V. V. Mikhailin and A. N. Vasil'ev, *IEEE Trans. Nucl. Sci.*, 2012, **59**, 2057–2064.
- A. Belsky, K. Ivanovskikh, A. Vasil'ev, M.-F. Joubert and C. Dujardin, *J. Phys. Chem. Lett.*, 2013, **4**, 3534–3538.
- D. R. Cooper, D. Bekah and J. Nadeau, *Front. Chem.*, 2014, **2**, year.
- H. Matsudaira, A. Ueno and I. Furuno, *Radiat. Res.*, 1980, **84**, 144–148.
- J. Hainfeld, D. Slatkin and H. Smilowitz, *Phys. Med. Biol.*, 2004, **49**, N309–N315.
- J. F. Hainfeld, F. A. Dilmanian, D. N. Slatkin and H. M. Smilowitz, *J. Pharm. Pharmacol.*, 2008, **60**, 977–985.
- S. Cho, *Phys. Med. Biol.*, 2005, **50**, N163–N173.
- S. J. McMahon, M. H. Mendenhall, S. Jain and F. Currell, *Phys. Med. Biol.*, 2008, **53**, 5635–5651.
- K. Kobayashi, N. Usami, E. Porcel, S. Lacombe and C. Le Sech, *Mutat. Res.-Rev. Mutat.*, 2010, **704**, 123–131.
- A. Garcia-Murillo, C. Le Luyer, C. Dujardin, T. Martin, C. Garapon, C. Pedrini and J. Mugnier, *Nucl. Instrum. Meth. A*, 2002, **486**, 181–185.
- J.-L. Bridot, A.-C. Faure, S. Laurent, C. Riviere, C. Billotey, B. Hiba, M. Janier, V. Josserand, J.-L. Coll, L. Vander Elst, R. Muller, S. Roux, P. Perriat and O. Tillement, *J. Am. Chem. Soc.*, 2007, **129**, 5076–5084.
- S. A. Osseni, S. Lechevallier, M. Verelst, C. Dujardin, J. Dexpert-Ghys, D. Neumeyer, M. Leclercq, H. Baaziz, D. Cussac, V. Santran and R. Mauricot, *J. Mater. Chem.*, 2011, **21**, 18365–18372.
- A. Alivisatos, *Science*, 1996, **271**, 933–937.
- D. Norris and M. Bawendi, *Phys. Rev. B*, 1996, **53**, 16338–16346.
- A. Guzelian, J. Katari, A. Kadavanich, U. Banin, K. Hamad, E. Juban, A. Alivisatos, R. Wolters, C. Arnold and J. Heath, *J. Phys. Chem.*, 1996, **100**, 7212–7219.
- O. Micic, H. Cheong, H. Fu, A. Zunger, J. Sprague, A. Mascarenhas and A. Nozik, *J. Phys. Chem. B*, 1997, **101**, 4904–4912.
- S. E. Letant and T. F. Wang, *Nano Lett.*, 2006, **6**, 2877–2880.
- A. Samia, X. Chen and C. Burda, *J. Am. Chem. Soc.*, 2003, **125**, 15736–15737.
- A. Samia, S. Dayal and C. Burda, *Photochem. Photobiol.*, 2006, **82**, 617–625.
- C. M. Lemon, E. Karnas, M. G. Bawendi and D. G. Nocera, *Inorg. Chem.*, 2013, **52**, 10394–10406.
- J. H. Hubbell and S. M. Seltzer, *NIST Standard Reference Database 126*, 1996.
- S. J. McMahon, W. B. Hyland, M. F. Muir, J. A. Coulter, S. Jain, K. T. Butterworth, G. Schettino, G. R. Dickson, A. R. Hounsell, J. M. O'Sullivan, K. M. Prise, D. G. Hirst and F. J. Currell, *Sci. Rep.*, 2011, **1**, year.
- J. Fang, H. Nakamura and H. Maeda, *Adv. Drug Deliver. Rev.*, 2011, **63**, 136–151.
- H. Huang and J. Hainfeld, *Int. J. Nanomed.*, 2013, **8**, 2521–2532.
- E. D. Bourret-Courchesne, G. A. Bizarri, R. Borade, G. Gundiah, E. C. Samulon, Z. Yan and S. E. Derenzo, *J. Cryst. Growth*, 2012, **352**, 78–83.